Journal of Materials Chemistry C

ROYAL SOCIETY OF CHEMISTRY

PAPER

View Article Online
View Journal | View Issue

Cite this: J. Mater. Chem. C, 2025, 13, 20085

High conductivity poly(ionic liquid)-based crosslinked dielectrics

Sophia McKillop, [a] Laura E. Dickson, [a] Hyungjun Cho, [a] May Ourabi, [a] Joseph G. Manion, [a] Vittoria-Ann DiPalo [a] and Benoît H. Lessard *[ab]

Received 28th May 2025,
Accepted 30th August 2025

DOI: 10.1039/d5tc02087e

rsc.li/materials-c

A wide range of emerging applications, from organic electronics to batteries, require dielectrics that offer high ionic conductivity while preventing hazards associated with dielectric leakage. Poly(ionic liquids) (PILs) are a promising class of materials which combine the high ionic conductivity of ionic liquids with the desireable mechanical properties of polymers. When developing thin film devices the deposition of multiple layers may necessitate orthoganol processing, limiting the choice of processing solvents and device designs. We developed a PIL that can be crosslinked with bis(2-bromoethyl) ether (BBEE) for use as a high performing dielectric. Electrochemical impedance spectroscopy was used to establish structure–property relationships. We investigated the effect of poly(ethylene glycol) methacrylate ion conducting monomers (mPEGMA) and 2-(dimethylamino)ethyl methacrylate (DMAEMA) composition in the PIL, the alkylation percentage in the PIL, and amount of BBEE to PIL on corresponding metal–insulator–metal capacitor performance. A balance between polymer composition and BBEE composition was identified to produce a robust PIL dielectric with a high electrical double layer (EDL) onset frequency and high capacitance density that is a solid at room temperature. The optimized PIL dielectric was then successfully integrated into a proof-of-concept solution-processed organic thin-film transistor (OTFT).

Introduction

Flexible and lightweight electronics for smart packaging offer considerable potential for addressing pressing global issues, such as reducing the estimated 1.3 billion tonnes of food wasted annually.[1] Realizing the widespread application of these technologies hinges on optimizing both the design of the electronic components, such as transistors, and the materials from which they are made. Organic thin-film transistors (OTFTs) are logic-gate operators or electrical switches that use carbon-based semiconductors such as conjugated polymers or small molecules in place of traditional inorganic semiconductors. OTFTs enable the design of complex circuits and sensors that can be integrated into flexible substrates and have the potential for low energy processing and large area manufacturing. For lightweight electronics and smart packaging, low operating voltage devices with reduced power consumption are critical to reduce the size of the required batteries.[2,3] Electrolyte-based or ionic liquid-based dielectric materials, where mobile ions can migrate during device operation to form electrical double layers (EDLs), enable thickness-independent capacitance that reduces device operating voltage (V_T).[4] However, during OTFT operation, the ions will diffuse into the semiconductor, slowing their return to the dielectric and leading to slow operating speed in a phenomenon known as electrochemical doping.[5,6] Electrolytes are also often toxic and can leak or leach into the environment upon device damage or at their end of life, limiting their use in applications where the device is in contact with skin or food.[6–8]

Poly(ionic liquids) (PILs) combine solid-state operation at room temperature with high ionic conductivity. In OTFTs they also limit electrochemical doping as the ions are bound to the polymer chain, preventing their diffusion into the semiconductor.[9–11] It is known that a PIL's molecular structure and architecture influence both the electrical and mechanical properties of the resulting thin film.[12] Block copolymer-based PILs can be an effective strategy to optimize switching speed, ionic conductivity, capacitance density, and mechanical stability by utilizing one block as a soft ion conducting domain while another provides a mechanically stable matrix.[13,14] While promising, many of the monomers and block copolymers used to create these dielectrics require multi-step, overly-complex synthetic routes. Additionally, PIL dielectrics can be limited by moisture sensitivity, suboptimal dielectric constants, and challenges with interfacial adhesion.

In previous work by Tousignant *et al.*, we prepared poly(2-(methacryloyloxy)ethyl trimethylammonium bis(trifluoromethylsulfonyl)azanide)-based PILs for use in OTFTs through a simple quaternization and subsequent counterion exchange at

[a] Department of Chemical and Biological Engineering, University of Ottawa, 161 Louis Pasteur, Ottawa, ON, Canada. E-mail: benoit.lessard@uottawa.ca
[b] School of Electrical Engineering and Computer Science, University of Ottawa, 800 King Edward Ave., Ottawa, ON, Canada

copolymers prepared with commercially available 2-(dimethylamino)ethyl methacrylate (DMAEMA) monomers.[15] By varying the copolymer composition, we could influence the frequency-dependent EDL formation which would dictate the operating frequency of the corresponding OTFTs. The corresponding devices were promising but suffered from low conductivity due to the polymers' high glass transition temperatures (T_g). Furthermore, these polymers required orthogonal solvent processing to minimize redissolution and washing off of the PIL during semiconductor deposition.

To overcome these issues, we designed a new PIL composed of poly(ethylene glycol) methyl ether methacrylate (mPEGMA) ion-conducting monomers and DMAEMA. We synthesized a series of statistical copolymers containing styrene and different ratios of mPEGMA and DMAEMA to enable optimization of both the T_g and ionic conductivity. The incorporation of mPEGMA reduces the T_g of the resulting polymers and confers ion transport capabilities to the PIL. DMAEMA contributes reactive sites which can undergo quaternization with di-bromo alkanes, leading to ionically charged species and enables crosslinking of the deposited film. Styrene was used to improve control of the polymerization.[16] The mPEGMA:DMAEMA ratios deployed in polymer syntheses were 10/90, 30/70, 50/50, 70/30 and 90/10. A portion of Poly(mPEGMA-DMAEMA-Sty) was partially alkylated by reacting the DMAEMA functional groups with *n*-propyl bromide for an alkylation range of 0 to 95%.

Abbasi *et al.* recently investigated the crosslinking of copolymers with 50 mol% of DMAEMA comonomer content, using bis(2-bromoethyl) ether (BBEE) in quaternation reactions. They found that a BBEE to DMAEMA ratio of 0.1 was sufficient to provide a high degree of crosslinking.[17] In this study we leveraged this crosslinking reaction to form robust PIL dielectrics for applications in organic electronics. BBEE content and mPEGMA:DMAEMA ratios in the copolymers were correlated to demonstrate that crosslinking of the thin films is directly related to EDL formation and conductivity of the capacitors. The crosslinked dielectrics were then integrated into bottom-gate top-contact (BGTC) OTFTs using semiconducting single-walled carbon nanotubes (sc-SWCNTs) as an air-stable semiconductor.

Results and discussion

Synthesis and crosslinking poly(mPEGMA-DMAEMA-Sty)

A series of poly(mPEGMA-DMAEMA-Sty) copolymers, denoted by $P_VD_WS_X$-CL_Y-A_0, were synthesized *via* nitroxide-mediated polymerization (NMP) using BlocBuilder-MA and styrene with different compositions of mPEGMA and DMAEMA (Table 1). NMP is an effective technique for the synthesis of well-defined polymers, providing narrow molecular weight distribution which can be integrated into organic electronics without the need for excessive purification beyond precipitation.[15,18–21] Using unimolecular initiators, NMP can synthesize a wide range of styrenics, acrylamides, acrylates and even methacrylates under specific conditions.[22–26] Copolymer composition and molecular weight characteristics such as number average molecular weight (M_n) and polymer dispersity ($Đ$) are in Tables S1, S2 and Fig. S1–S3. The polymers were synthesized to a M_n of 31 to 67 kg mol^{-1} with a $Đ$ between 1.6–2.2, which is typical for NMP of methacrylates when copolymerized with a small amount of styrene (Table 1 and Fig. 1).[17,27,28] Similar crosslinking chemistry with poly(mPEGMA-DMAEMA-Sty) was performed within the range of 0 to 0.5 molar equivalents of BBEE to DMAEMA.

Table 1 Summary of characteristics of capacitors of $P_VD_WS_X$-CL_Y-A_Z including EDL onset, capacitance density at 0.01 Hz and 10 Hz, and conductivity

Film ID	EDL onset (Hz)	C_i at 10 Hz (μF cm^{-2})	C_i at 0.01 Hz (μF cm^{-2})	Conductivity (S cm^{-1})
$P_{10}D_{87}S_3$-CL_0-A_0	12.589	0.01 ± 0.003	2.63 ± 1.86	2.26×10^{-10}
$P_{28}D_{69}S_3$-CL_{10}-A_0	25.116	0.02 ± 0.013	6.34 ± 2.67	1.12×10^{-9}
$P_{50}D_{48}S_2$-CL_{10}-A_0	501.19	1.02 ± 0.201	9.35 ± 1.31	1.50×10^{-8}
$P_{68}D_{29}S_3$-CL_{10}-A_0	794.33	1.57 ± 0.762	7.57 ± 1.39	2.68×10^{-8}
$P_{87}D_{10}S_3$-CL_{10}-A_0	—	—	—	—
$P_{50}D_{48}S_2$-CL_{10}-A_{25}	15 849	4.89 ± 0.779	15.49 ± 2.93	3.33×10^{-7}
$P_{50}D_{48}S_2$-CL_{10}-A_{50}	31 623	4.15 ± 0.817	11.90 ± 2.24	8.20×10^{-7}
$P_{50}D_{48}S_2$-CL_{10}-A_{75}	125 890	4.56 ± 0.760	16.08 ± 3.08	1.58×10^{-5}
$P_{50}D_{48}S_2$-CL_{10}-A_{85}	2511.9	2.08 ± 0.822	7.18 ± 1.39	7.03×10^{-8}
$P_{50}D_{48}S_2$-CL_{10}-A_{95}	—	—	—	—

Raman spectroscopy was used to study the crosslinked films of $P_{50}D_{48}S_2$-CL_Y-A_0. The polymer was dissolved in acetonitrile (ACN) and combined with 0 to 0.9 molar equivalents of BBEE per DMAEMA unit (Fig. 1(iii)). The polymer/BBEE solution was used to cast films and then heated to crosslink the polymer chains. The Raman spectra between 2700 to 3200 cm^{-1} was examined as the methyl and methylene functional groups associated with the quaternization reaction are found within this region.[29–31] The extent of crosslinking in the films upon quaternization with BBEE was monitored through the –CH_3 vibration in the –N–$(CH_3)_2$ group of DMAEMA.[31] The Raman peak associated with this group has been assigned to the peak occurring at ∼2825 cm^{-1} which is within the known literature range.[29,31] In the films of $P_{50}D_{48}S_2$-CL_0-A_0, which have 0 molar equivalents of BBEE there is a peak at ∼2825 cm^{-1} that downshifts to 2820 cm^{-1} with increasing crosslinker content (Fig. 2(F)). This peak shift is consistent with a change in the environment and with a mix of species (reacted/unreacted).

Other notable Raman signals appear at 2875 cm^{-1} and 2965 cm^{-1}, corresponding to the –CH_3 symmetric and antisymmetric vibrations of the DMAEMA monomer, respectively. Weaker bands are observed at 2933 cm^{-1} and 3043 cm^{-1}, associated with –CH and –CH_2 vibrations.[29–31] In particular, the –CH_2 vibration was monitored because the quaternization reaction is expected to increase the Raman intensity of this signal due to the methylene units of the BBEE crosslinker. Consistent with this, increasing crosslinker content produces a shoulder near 2933 cm^{-1}, suggesting a growing concentration of these units upon quaternization (Fig. 2(A)–(D)). This trend is further supported by the rising intensity ratio of the –CH_2 to –CH_3 antisymmetric stretches, which increases with BBEE content until plateauing at 0.5 equivalents of BBEE per DMAEMA

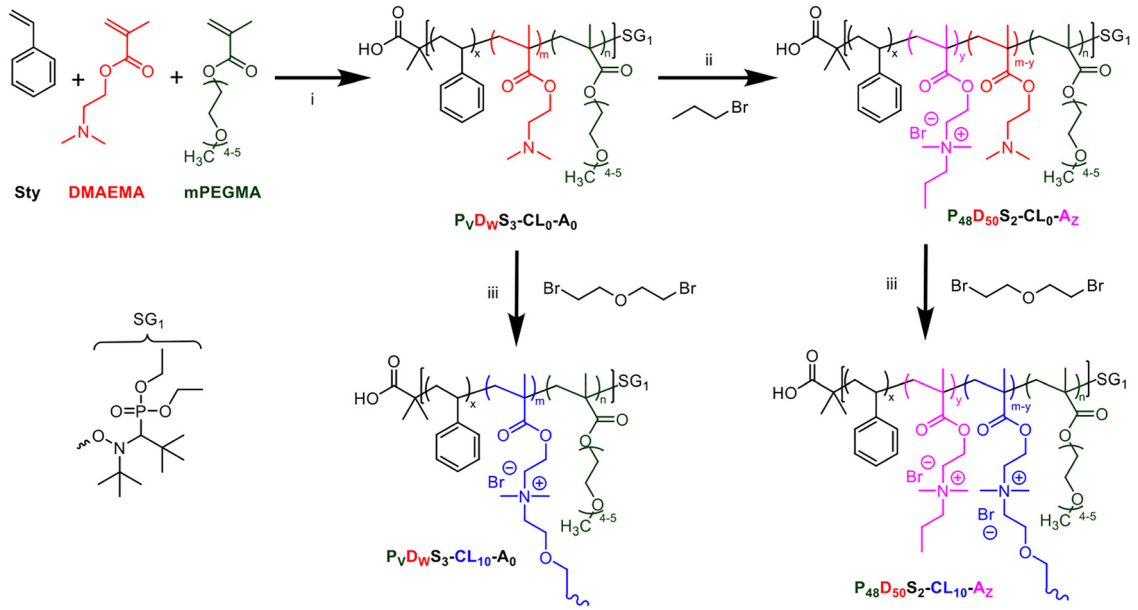

Fig. 1 Synthesis pathway of poly(mPEGMA-DMAEMA-Sty), (i) dissolved in toluene SG_1 (BlocBuilder-MA) and put in an ice bath for 15 min bubbled with N_2 then heated and stirred at 90 °C for 60 min, (ii) alkylation reaction of $P_{50}D_{48}S_2CL_0A_0$ by adding desired molar equivalent of *n*-propyl bromide in acetonitrile stirring at room temperature overnight, (iii) crosslinking reaction of polymer with desired molar equivalent of BBEE to DMAEMA coated and annealed at 80 °C overnight and increased to 100 °C for 1 hour.

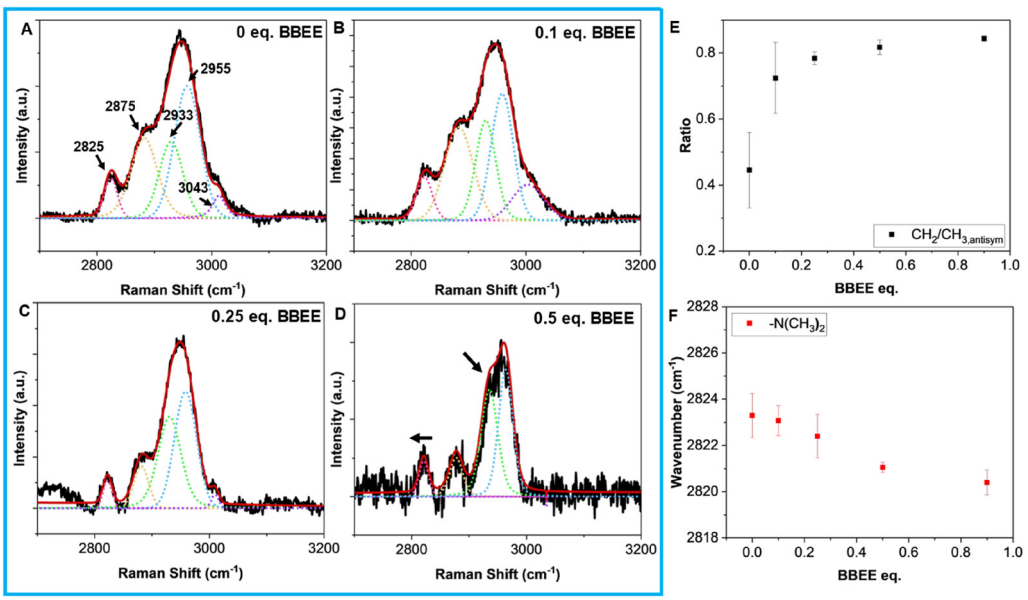

Fig. 2 (A)–(D) Raman spectra $P_{50}D_{48}S_2$-CL_Y-A_0 crosslinking (black) together with the results of fitted peak analysis (red) of five mixed Lorentz–Gaussian functions (pink, yellow, green, blue, and purple) for 0, 0.1, 0.25, and 0.5 molar eq. BBEE to DMAEMA monomer units. (E) $-CH_2/-CH_3$, antisymmetric ratio and (F) $-N(CH_3)_2$ Raman peak wavenumber plotted against BBEE molar equivalent to DMAEMA monomer units.

monomer unit (Fig. 2(E)).[32] As the films are vacuum annealed above the boiling point of BBEE prior to their evaluation we anticipate that any residual, unreacted crosslinker should be removed and therefore the observed increase in methylene signal is likely due to increased crosslinking or partial alkylation by BBEE.

Increasing the molar equivalent BBEE content past 0.5 appears to result in stabilization of the $-N-(CH_3)_2$ peak wavenumber and $-CH_2/-CH_3$, antisymmetric ratio, indicating that the degree of crosslinking is limited to this molar equivalent of crosslinker (Fig. S4). Indeed, exceeding 0.5 eq. crosslinker can result in crosslinking suppression due to the bifunctionality of

BBEE. Therefore, we surmise the high degree of quaternization associated with high crosslinker content inhibits further quaternization, resulting in minimal shifts to the Raman spectra.

Crosslinked PIL dielectrics integration in MIM capacitors

MIM capacitors were fabricated on glass substrates using $P_VD_WS_X$-CL_Y-A_Z sandwiched between gold electrodes and were characterized by impedance spectroscopy over a frequency range of 10^6 to 0.01 Hz. Fig. 3(A) demonstrates the capacitance density as a function of frequency as well as the phase angle as a function of frequency. The mPEGMA:DMAEMA ratio in the polymer ranges from 10/90, 30/70, 50/50, 70/30, and 90/10. Each film was crosslinked with 0.1 equivalent of BBEE to DMAEMA present in the polymer for film formation. $P_{87}D_{10}S_3$-CL_{10}-A_0 (~90%mPEGMA) had poor film formation which led to non-functional sites which is why it is not presented in Fig. 3(A).

Electrolytic dielectric material performance is characterized by EDL formation and the frequency at which the EDL onset occurs. The initial decrease in the phase angle, from 90° to 45°, is indicative of the dipolar relaxation regime where the polymer chains start aligning with the applied electric field. This was used to identify when the EDL began to form and was reported as the EDL onset frequency.[33] As the phase angle decreases below 45° the ionic relaxation regime is entered, in which mobile ions begin migrating towards the positively or negatively charged electrodes.[33] The phase angle increases above 45° again, which is considered the EDL formation regime, and the EDL is considered fully formed once the phase angle curve plateaus.[33] This phenomenon was used to evaluate the corresponding PILs. An overall trend was observed: as the mPEGMA content increased the capacitance density and the EDL onset frequency both increased (Fig. 3(A)). The EDL onset was found to shift from 1.26×10^1 to 7.94×10^2 Hz as the mPEGMA content increased in the polymers (Table 1). Additionally, the maximum capacitance density at 0.01 Hz was found to increase from 2.63 to 7.57 μF cm^{-2} as the mPEGMA content increased (Table 1 and Fig. 3). The capacitance density of $P_{10}D_{87}S_3$-CL_{10}-A_0, $P_{28}D_{69}S_3$-CL_{10}-A_0, $P_{50}D_{48}S_2$-CL_{10}-A_0, and $P_{68}D_{29}S_3$-CL_{10}-A_0 are comparable to other PIL MIM capacitors, as previously reported by our group, where Tousignant *et al.* investigated PILs containing 35 and 62 mol% DMAEMA in copolymers with methyl methacrylate resulting in capacitance densities of 1.15 and 1.78 μF cm^{-2}, respectively.[15] In another study by our group Peltekoff *et al.* explored PIL block copolymers of poly(styrene)-*b*-poly(1-(4-vinylbenzyl)-3-butylimidazolium-*random*-poly(ethylene glycol) methyl ether methacrylate) (poly(S)-*b*-poly(VBBI$^+$[X]-*r*-PEGMA)) with varying PEGMA/VBBI$^+$ ratios and three different mobile anions (where X = $TFSI^-$, PF_6^- or BF_4^-), and reported capacitance densities between 0.02 to 10 μF cm^{-2}. Similarly, Peltekoff *et al.* found that capacitance density and EDL onset frequency increased with mPEGMA content.[13] PILs with higher mPEGMA content stored more charge and were better able to align the dipoles in response to an electric field, allowing for ions to move quickly and easily through the film.[13] The same is thought to explain the results presented in Table 1, however, increasing the mPEGMA content past 70% led to non-functional devices highlighting the tradeoff between high performance and overall device reliability.

The ionic conductivity of $P_{10}D_{87}S_3$-CL_{10}-A_0, $P_{28}D_{69}S_3$-CL_{10}-A_0, $P_{50}D_{48}S_2$-CL_{10}-A_0, and $P_{68}D_{29}S_3$-CL_{10}-A_0 was determined using

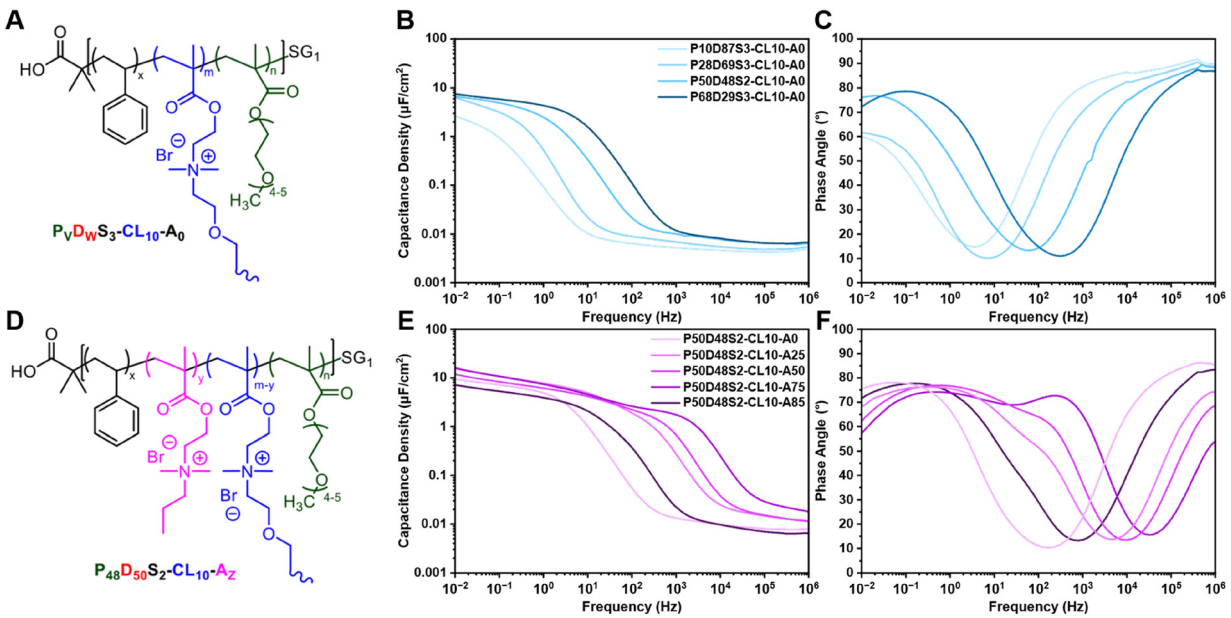

Fig. 3 Electrochemical impedance spectroscopy (EIS) results of the effect of changing mPEGMA to DMAEMA ratio in P_VD_W-CL_{10}-A_0 and effect of alkylation of $P_{48}D_{50}S_2$-CL_{10}-A_Z (A) chemical structure of $P_VD_WS_X$-CL_YCL_{10}-A_0, (B) capacitance density *vs.* frequency of mPEGMA to DMAEMA ratio in $P_VD_WS_X$-CL_YCL_{10}-A_0, (C) phase angle *vs.* frequency of mPEGMA to DMAEMA ratio in $P_VD_WS_X$-CL_YCL_{10}-A_0. The legend used in (B) is the same for (C). Results for $P_{87}D_{10}S_3$-CL_{10}-A_0 was not included due to poor film formation. (D) chemical structure of $P_{50}D_{48}S_2$-CL_{10}-A_Z, (E) capacitance density *vs.* frequency of effect of alkylation of $P_{50}D_{48}S_2$-CL_{10}-A_Z, (F) phase angle *vs.* frequency of effect of alkylation of $P_{50}D_{48}S_2$-CL_{10}-A_Z. The legend used in (E) is the same for (F).

parallel resistance of the circular fit from the semi-circle portion of the Nyquist plot from EIS (Fig. S5). The conductivities were determined to be between 2.26×10^{-10} to 2.68×10^{-8} S cm^{-1} (Table 1). The results presented in this work are comparable to other previously reported results by Tousignant *et al.* with conductivities between 3.47×10^{-11} to 1.78×10^{-9} S cm^{-1} and Peltekoff *et al.* with conductivities ranging from 5.8×10^{-11} to 3.4×10^{-7} S cm^{-1}.[13,15]

The amount of BBEE to DMAEMA was investigated to optimize the crosslinker to DMAEMA in the copolymer through integration into capacitors (Fig. S6 and Table S4). Various ratios of BBEE to DMAEMA, from 0, 0.1, 0.25, and 0.5 molar equivalents of BBEE, were explored. The capacitance density at 10 Hz was found to be 0.02 and 2.08 μF cm^{-2}, for 0 and 0.1 molar equivalents of BBEE respectively. Molar equivalents of BBEE $\geq$0.25 led to poor film formation and significant roughness (Tables S2 and S3) resulting in inconsistent and non-functional devices. Therefore, the optimal amount of crosslinker was determined to be 0.1 molar equivalents of BBEE relative to DMAEMA for all samples.

Pre-alkylation of DMAEMA containing polymers

We surmised that with 0.1 molar equivalents of BBEE to DMAEMA, not all the DMAEMA units are being reacted and would still be available for functionalization. Therefore, we performed an alkylation step to $P_{50}D_{48}S_2$-CL_0-A_0 by quaternization of the initial polymer with *n*-propyl bromide prior to crosslinking in the films (Table 1 and Fig. 1). The ratio of *n*-propyl bromide was calculated to different molar ratios relative to the available DMAEMA sites. The percentage of alkylation to DMAEMA in the polymers ranges from 0, 25, 50, 75, and 85%. We wanted to only partially alkylate copolymers to ensure that DMAEMA sites were still available for crosslinking with BBEE. For example, $P_{50}D_{48}S_2$-CL_{10}-A_{95}, alkylation of 95% was attempted and did not produce functional devices which we associated to full quaternization and in turn a lack of crosslinking sites available in the polymers, leading to soft sticky films. Capacitors were therefore fabricated with the alkylated series of polymers, with the addition of 0.1 molar equivalent of BBEE (Fig. 3(B), and Table 1). Overall, the pre-alkylation led to an increase in capacitance density, EDL onset frequency, and conductivity compared to the non-alkylated polymers with identical compositions (Table 1). The EDL onset was found to range from 5.01×10^2 to 1.26×10^5 Hz and the maximum capacitance density at 0.01 Hz was found to be 16.08 μF cm^{-1} for $P_{50}D_{48}S_2$-CL_{10}-A_{75}; which is roughly 9 times greater than previous reports using alkylated P(DMAEMA-ran-MMA) PIL dielectrics and roughly 54 times greater than poly(S)-*b*-poly(VBBI$^+$[X]-*r*-PEGMA), block copolymers with TFSI$^-$.[13,15]

The ion conductivity for $P_{50}D_{48}S_2$-CL_{10}-A_X was determined from a circular fit of the semi-circle portion of the Nyquist plot from EIS. Ionic conductivity was determined to be as high as 1.59×10^{-5} S cm^{-1} for $P_{50}D_{48}S_2$-CL_{10}-A_{75}, which is roughly 8000 times greater than previous reports using alkylated P(DMAEMA-*ran*-MMA) PIL dielectrics and roughly 46 times greater than poly(S)-*b*-poly(VBBI$^+$[X]-*r*-PEGMA), block copolymers with TFSI$^-$; clearly demonstrating the importance of alkylation of the pre-polymer prior to crosslinking (Table 1).[13,15] An overall trend was observed: an increase in alkylation up to 75% of the DMAEMA repeat units led to an increase in ion conductivity, capacitance density, and EDL onset frequency. This suggests that the increase in alkylation up to this point allows for more ions to be present within the film, which leads to more ions moving through the film. This enables the film to form the EDL at higher frequencies and possess higher conductivity. The alkylation of the prepolymer leads to the quaternization of the crosslinkable DMAEMA repeat units and as a result minimal crosslinking occurs. This may give the film the high conductivity desired as well as flexibility due to crosslinking suppression due to the alkylation. Moreover, the capacitance density of devices made with $P_{50}D_{48}S_2$-CL_{10}-A_{85} decreased dramatically, suggesting that the resulting films were too soft and there were insufficient DMAEMA sites for the crosslinking reaction to take place. Beyond the performance metrics, the film's properties differ in that its polymer matrix contains fewer partially crosslinked crosslinkers and presumably little to no free DMAEMA sites. The tertiary amine groups of free DMAEMA are electron-donating moieties known to impact OTFT device performance.[34]

Crosslinked PIL dielectric integration into organic thin film transistors

Proof-of-concept n-type bottom gate top contact (BGTC) OTFTs were fabricated on Si substrates with $P_{68}D_{29}S_3$-CL_{10}-A_{25} as the dielectric layer combined with sc-SWCNT as the semiconducting layer. Sc-SWCNTs were selected due to their good mechanical properties, solution processability, and high current carrying capacity leading to OTFTs with high transconductance even when paired with polymer dielectrics.[18,34–38] Recently, we integrated sc-SWCNTs into proof-of-concept OTFTs using bio-based dielectrics such as chitosan.[39,40] Building on this, the crosslinked PILs from this work were integrated into OTFTs, with characteristic output and transfer curves reported in Fig. 4.

When operating in the linear regime, device performance from 5 devices was found to have an average $I_{ON/OFF}$ of 25, a V_T of 1.65 V $\pm$ 0.10, and a transconductance of 0.72 μS $\pm$0.41 (Table S6). The devices showed negligible hysteresis, but significant leakage current is observed, which is attributed to the high conductivity of the $P_{68}D_{29}S_3$-CL_{10}-A_{25} dielectric.[41] The V_T of the $P_{68}D_{29}S_3$-CL_{10}-A_{25} with sc-SWCNT OTFTs presented in this work is comparable to other PIL dielectrics integrated into OTFTs, reporting operating voltages of 1.1 to 2.7 V for P(METATFSI-MMA) PILs when paired with sc-SWCNTs.[15] Similarly, when 1-butyl-3-methylimidazolium 1-[3-(methacryloyloxy) pro-pylsulfonyl]-1-(trifluoromethanesulfonyl)imide and mPEGMA-based block copolymers are paired in a device with sc-SWNTs, a threshold voltage of 1.1 V can be achieved.[42] However, in both cases, device architecture was top gate bottom contact while this study integrates the material in a bottom gate top contact architecture. This highlights the orthogonal processability of these dielectric materials and illustrates that incorporating crosslinking in the dielectric layer enables more flexibility in the fabrication of OTFTs.

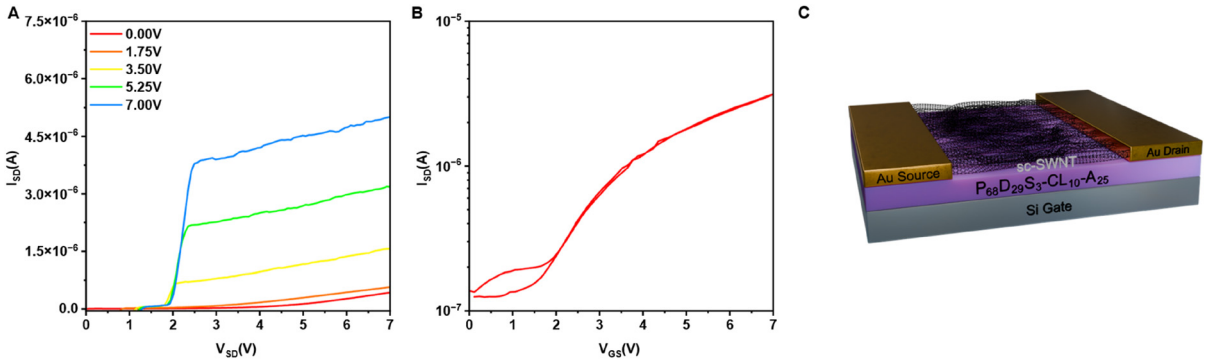

Fig. 4 Characteristic (a) output, (b) transfer curves for BGTC OTFTs prepared using $P_{68}D_{29}S_3$-CL_{10}-A_{25} with sc-SWCNTs. The transfer curve was operated at a V_{SD} of 3V, and the average of the last measurement of five transfer curves is presented to ensure the film is appropriately charged (c) BGTC device architecture.

Experimental

Materials

Styrene (S4972, ≥99%), poly(ethylene glycol) methyl ether methacrylate (mPEGMA, 447935, ≤100%), 2-(dimethylamino)ethyl methacrylate (DMAEMA, 234907, 98%), acetonitrile (ACN, 271 004, ≥99.8%), aluminum oxide (199 443, Brockmann I, activated, basic with <0.03% Fe_2O_3, <0.4% Na_2O), hexanes (227 064, ≥99%), and dichloromethane (DCM, 270 997, ≥99.8%) were purchased from Millipore-Sigma. BlocBuilder-MA (HES1179) was kindly donated by Marc Dubé (University of Ottawa), who received it from Arkema. Toluene (92030-2-10, ≥99.5%) was purchased from Caledon. *N*,*N*-Dimethylformamide (DMF, 99.9% HPLC grade), bis(2-bromoethyl) ether (BBEE, 005451, 97%) and *n*-propyl bromide (BR1117, 99%) were purchased from Oakwood Chemical. Plasma torch carbon nanotubes were purchased from Raymor NanoIntegris (RNB781-120). Poly(9,9′-didodecyl-fluorene-*co*-*N*-(2′-decyltetradecane)-carbazole) (PCPF) was received from the Adronov Research Group at McMaster University. All chemicals and reagents were used as received unless otherwise specified.

Preparation of sc-SWCNT dispersion

Pure dispersions of semiconducting single-walled carbon nanotubes were prepared using conjugated polymer sorting, as reported in our previous work.[18] Briefly, the conjugated polymer, PCPF, and raw nanotubes were added to 20 mL of toluene in a 0.8 : 1 ratio and sonicated for 90 minutes. The dispersions were then centrifuged, and the supernatants were combined to create a stock solution.

Synthesis of poly(mPEGMA-DMAEMA-Sty)

Poly(mPEGMA-DMAEMA-Sty) was synthesized through nitroxide mediated polymerization (NMP) following previously reported synthesis procedures for NMP.[19–21,43,44] The molar ratio of BlocBuilder-MA and of mPEGMA, DMAEMA, and styrene was calculated to provide a target number average molecular weight of $M_{n,Target}$ = 67 kg mol^{-1}. As an example, or $P_{50}D_{48}S_2$-CL_{10}-A_0 BlocBuilder-MA (0.07 g, 0.19 mmol), mPEGMA(5.70 g, 19.00 mmol), DMAEMA (2.99 g, 19.00 mmol), and styrene (0.12 g, 1.14 mmol) were added to 8.25 mL toluene and bubbled with N_2 in an ice bath for 15 minutes (Table S1). The solution was then heated in a sand bath at 90 °C for 60 minutes to allow for polymerization to occur. An aliquot of polymerization mixture was taken for analysis with ^{1}H-NMR to determine monomer conversion for each polymer before precipitation and isolation of the polymer (Fig. S1). The polymer was isolated by precipitation in 100 mL hexanes, decanted, then redissolved in 2.5 mL DCM, this was repeated 3 times. The polymer dissolved in DCM was dried and analyzed through size exclusion chromatography (SEC) and ^{1}H-NMR. Analysis by SEC including M_n and $Đ$ for each polymer is presented in Table S2. The polymer size and size dispersity were analyzed by gel permeation chromatography (GPC) with DMF as the eluent. The eluent was pumped by Malvern Omnisec Resolve at a flow rate of 1.0 mL min^{-1} at 40 °C. The sample passed through a guard column (DGuard, Org Guard, 10 × 4.6 mm) and then two analytical columns in series (two D6000M, General mixed org, 300 × 8.0 mm). The sample was analyzed using a MALS detector, (Malvern Viscotek SEC-MALS 20), RI & UV/vis detectors (Malvern Omnisec Reveal). PS standards (105 kDa and 245 kDa) were used to perform multi-detector calibration. The ^{1}H-NMR analysis showed peaks at 4.0–3.3 ppm (HC–O–R from mPEGMA), 2.0–2.7 ppm (O–CH_2 from DMAEMA), and 6.9–7.25 ppm aromatic rings from styrene were used to determine the polymer molar composition (F_S, F_{DMAEMA} and F_{mPEGMA}). The styrene peaks at 6.9–7.3 ppm was assumed to represent 3 repeats for 3 mol% composition since styrene conversion was complete, thus, integration value of 15 was assigned. The ^{1}H-NMR spectra were obtained by using a Bruker AVANCE II 400 MHz spectrometer. The ^{1}H-NMR spectrum and SEC results are presented in Fig. S1 and S2. For $P_{50}D_{48}S_2$-CL_{10}-A_0 the polymerization conversion was 54% with a final M_n = 67 kg mol^{-1}, $Đ$ = 1.5 and F_{DMAEMA} = 0.48, F_{mPEGMA} = 0.50.

Alkylation of poly(mPEGMA-DMAEMA-Sty)

The polymer (0.5 g) was dissolved in can (3 mL) equipped with a stir bar. The percentage (25%, 50%, 75%, 85%, 95%) per DMAEMA molar ratio of *n*-propyl bromide to DMAEMA units was added to the flask containing the polymer solution (Table S3). The solution was left stirring at room temperature

overnight. The stir bar was removed, the excess solvent was rotovapped, and the sample was dried *in vacuo* overnight and analyzed by ^{1}H-NMR. Broad peaks that appeared at 4.5 ppm indicated successful alkylation. ^{1}H-NMR spectra are presented in Fig. S3. Sample composition has been abbreviated as $P_VD_WS_X$-CL_Y-A_Z where V, W, X represent the percentage of mPEGMA, DMAEMA, and styrene respectively, Y represents the percentage of crosslinking, and Z represents the percentage of alkylation.

Preparation of dielectric solution

Each component of the dielectric solution including the polymer, ACN, and crosslinker were filtered through a 0.45 μm polytetrafluorethylene syringe filter prior to mixing. The dielectric solution was composed of 150 mg mL^{-1} of $P_VD_WS_X$-CL_Y-A_Z dissolved in ACN and 0.1 molar equivalent of the crosslinker, BBEE, per DMAEMA was added.

Fabrication and characterization of metal–insulator–metal (MIM) capacitors

25 mm × 25 mm glass substrates were submerged in the following sequence: detergent solution, DI water, acetone, and methanol for 5 minutes each and placed in an ultrasonication bath to be cleaned. The substrates were dried with a flow of nitrogen gas and transferred into the glovebox for the physical vapour deposition of the bottom electrodes. 2 nm of Cr followed by 50 nm of Au were patterned onto the substrates to create bottom electrodes using custom shadow masks. The dielectric solution prepared as previously described. The dielectric layer was fabricated by coating the solution on top of the bottom electrodes *via* spin-coating. 300 μL of dielectric solution was dispensed onto the substrate and spin-coated at 2000 rpm for 90 s. Once spin-coated, the substrates were annealed in an oven under vacuum at 80 °C overnight. The following morning, the oven temperature was increased to 100 °C for 1 hour and then cooled to room temperature before being removed from the oven. 50 nm of Au top electrodes were deposited on the substates through a shadow mask. Each substrate contained 10 capacitor sites with different areas, and each polymer sample used as a dielectric layer was fabricated in duplicates, resulting in a total of 20 capacitor sites per sample (n = 20).

Electrochemical impedance spectroscopy (EIS)

EIS was used to obtain the dielectric properties of the films which was achieved by sweeping frequency from 10^6 Hz to 0.01 Hz at 10 mV using a Metrohm PGSTAT204 potentistat/galvanostat. An average film thickness and root mean square roughness was calculated from six different measurements taken on each film using a Dektak XT profilometer (Bruker) (Table S5). Eqn (1) and (2) describe the dielectric constant (κ) and capacitance density (C_i) for each site which was calculated using the real (Z) and imaginary (Z'') portions of impedance, average film thickness (t), capacitor area (A), permittivity of vacuum (ε_0), and angular frequency (ω).

$$\kappa = \frac{t}{\omega A \varepsilon_0}\left(\frac{Z''}{Z''^2 + Z'^2}\right) \quad (1)$$

$$C_i = \frac{\kappa \varepsilon_0 A}{t} \quad (2)$$

EIS-derived real (Z) and imaginary (Z'') portions of impedance were used to calculate the parallel resistance from a circular fit of the semi-circle portion. This fit obtained the value of bulk resistance which was used to obtain ionic conductivity (σ) of the films using average film thickness (t), bulk resistance (R_b), and capacitor area (A) seen in eqn (3).

$$\sigma = \frac{t}{R_b A} \quad (3)$$

Raman spectroscopy of poly(mPEGMA-DMAEMA-Sty)

Raman spectra were recorded using Renishaw inVia InSpec confocal Raman microscope with a Leica Microsystems bright-field microscope with a DM2700 light source. A 500 mW 532 nm wavelength laser with a 2400 L mm^{-1} grading was used to measure the 2700–3500 cm^{-1} spectral range using 100× objective. Calibration was performed against a 520 cm^{-1} silicon reference peak within 0.5 cm^{-1}. Films for Raman spectroscopy were prepared on 20 mm × 15 mm Si wafers and were cleaned beforehand by sonication in detergent, DI water, acetone, and methanol for 5 minutes each. Films were fabricated as described previously. Raman spectra were taken in the middle of the sample with 10% laser power, an exposure time of 10 seconds, and 10 accumulations. The spectra were baseline corrected, and peak position was determined through the WiRE curve fitting software. Each spectrum was normalized between 0 and 1 to show the change in intensity between the various spectra.

Fabrication of OTFTs

OTFTs were fabricated on 20 mm × 15 mm Si wafers (WaferPro), cleaned as previously described for MIM capacitors. The dielectric used for MIM capacitors was used as the dielectric in the OTFT following the same spin coating and annealing procedure but instead onto an Si wafer and using 200 μL for spin coating. After annealing, SWCNTs were dropcast onto the substrate manually using a prepatterned guide for drop placement. 0.3 μL of SWCNT dispersions were drop-cast onto the substrate in each of the 20 prepatterned channel positions. After each drop of SWCNTs, the substrate was rinsed with 1 mL of toluene four times and dried with nitrogen between each rinse. This was repeated three times such that each OTFT channel received 3 drops of SWCNTs. Substrates were then annealed at 100 °C for 2 hours under vacuum. Gold top electrodes were deposited *via* PVD at 0.5 Å s^{-1} to a thickness of 50 nm through prepatterned Ossila shadow masks.

OTFTs were tested using a custom designed autotester connected to a Keithley 2614B source meter. The output and transfer curves for all 20 sites on the substrate were obtained using this autotester and a LabVIEW program.[45] Output curves were obtained by sweeping the source-drain voltage (V_{SD}) while maintaining a constant source-gate voltage (V_{GS}). Transfer curves were obtained in the linear regime by sweeping V_{GS} and maintaining a constant V_{SD}. Transconductance (g_m) and V_T

were modelled using the metal-oxide-semiconductor field-effect transistor (MOSFET) model as seen in eqn (4) and (5).

$$I_{SD} = \frac{W}{L}\mu C_i\left(V_{GS} - V_T - \frac{V_{SD}}{2}\right)V_{SD} \quad (4)$$

$$g_m = \frac{dI_{SD}}{dV_{GS}} \quad (5)$$

Conclusion

Crosslinking with BBEE and the tertiary amine present in the DMAEMA of the PIL was used to fabricate robust PILs for orthogonal solution processed bilayer devices with tunable capacitance and ionic conductivity. Raman spectroscopy showed a drop in wavenumber with increased BBEE content, suggesting increased crosslinking. PIL MIM capacitors were fabricated with the resulting robust films and demonstrated high capacitance density, high frequency EDL formation, and ionic conductivity. Moreover, increasing the ratio of mPEGMA in the PIL dielectric demonstrated an increase in capacitance density and EDL onset. Additionally, the pre-alkylation of the DMAEMA units of the PIL polymers led to a 3-order of magnitude increase in EDL onset formation and conductivity, as well as a 4× increase in capacitance density when pre-alkylating 75% of the DMAEMA monomers prior to crosslinking in the film.

The PIL was also incorporated into preliminary bottom gate top contact, solution processed OTFTs with sc-SWCNT semiconductors, achieving a threshold voltage of <1.6 V and performance characteristics comparable to other PIL dielectrics incorporated into OTFTs. Overall, this study demonstrates an effective strategy to develop robust highly conductive dielectrics for use in robust solution processed organic electronics.

Author contributions

The manuscript was written through the contributions of all authors. All authors have given approval to the final version of the manuscript. S. M: conceptualization, investigation, formal analysis, writing – original draft. S. M. conducted experimental work and data analysis, as well as wrote the initial draft of the manuscript. L. E. D.: investigation, methodology, data curation, writing – review and editing. L. E. D. assisted in the OTFT and Raman spectroscopy experiments and analysis. H. C: investigation, writing – review and editing. H. C. assisted in synthesis. M. O.: investigation, writing – review and editing. M. O. assisted in Raman spectroscopy experiments, and SWCNT preparation. J. G. M.: visualization, writing – review and editing. J. G. M. created OTFT figures. V. D.: analysis, writing – reviewing and editing. V. D. contributed to Raman spectroscopy analysis and manuscript editing. B. H. L.: funding acquisition, supervision, project administration, conceptualization, writing – review and editing. B. H. L. acquired funding, managed supervision, directed the study, and assisted in editing the manuscript.

Conflicts of interest

The authors declare no conflict of interest.

Data availability

The data supporting this article have been included as part of the SI. Supplementary information: NMR, GPC, Raman spectroscopy, EIS, OTFT, and additional synthesis data. See DOI: https://doi.org/10.1039/d5tc02087e.

Acknowledgements

We thank Natural Sciences and Engineering Research Council of Canada (NSERC) Discovery program (RGPIN-04079-2020 to B.H.L) for supporting this project and NSERC CGS (L.E.D and M.O.). We thank the Canadian Foundation for Innovation, CFI# 40178 (HIIT) and CFI# 43247 (SSMART), for support in acquisition and maintenance of the infrastructure needed for this project. We would like to thank Dr. Joseph G. Manion (CGFigures) for providing a figure element. The authors thank the Adronov Research Group from McMaster University for the synthesis of the PCPF polymer and professor Marc Dubé from the University of Ottawa for donating the BlocBuilder-MA from Arkema.

References

1 Food and Agriculture Organization of the United Nations (FAO), Global initiative on food loss and waste reduction, Rome, 2016.
2 S. Jakher and R. Yadav, *Microelectron. Eng.*, 2024, **290**, 112193.
3 Z. Hao, Z. Wu, S. Liu, X. Tang, J. Chen and X. Liu, *J. Mater. Chem. C*, 2024, **12**, 9427–9454.
4 H. Kim, Y. Won, H. W. Song, Y. Kwon, M. Jun and J. H. Oh, *Adv. Sci.*, 2023, **11**, 2306191.
5 L. G. Kaake, Y. Zou, M. J. Panzer, C. D. Frisbie and X.-Y. Zhu, *J. Am. Chem. Soc.*, 2007, **129**, 7824–7830.
6 J. D. Yuen, A. S. Dhoot, E. B. Namdas, N. E. Coates, M. Heeney, I. McCulloch, D. Moses and A. J. Heeger, *J. Am. Chem. Soc.*, 2007, **129**, 14367–14371.
7 S. Jin, D. Mu, Z. Lu, R. Li, Z. Liu, Y. Wang, S. Tian and C. Dai, *J. Cleaner Prod.*, 2022, **340**, 130535.
8 K. Du, E. H. Ang, X. Wu and Y. Liu, *Energy Environ. Mater.*, 2022, **5**, 1012–1036.
9 J. Li, W. Tang, Q. Wang, W. Sun, Q. Zhang, X. Guo, X. Wang and F. Yan, *Mater. Sci. Eng., R*, 2018, **127**, 1–36.
10 B. Nketia-Yawson and Y.-Y. Noh, *Adv. Funct. Mater.*, 2018, **28**, 1802201.
11 T. Fujimoto and K. Awaga, *Phys. Chem. Chem. Phys.*, 2013, **15**, 8983–9006.
12 L. G. T. Gaines, *Am. J. Ind. Med.*, 2023, **66**, 353–378.
13 A. J. Peltekoff, S. Brixi, J. Niskanen and B. H. Lessard, *JACS Au*, 2021, **1**, 1044–1056.
14 J. Niskanen, M. N. Tousignant, A. J. Peltekoff and B. H. Lessard, *Polymer*, 2021, **212**, 123144.

15 M. N. Tousignant, M. Ourabi, J. Niskanen, B. Mirka, W. J. Bodnaryk, A. Adronov and B. H. Lessard, *Flexible Printed Electron.*, 2022, **7**, 034004.
16 J. Nicolas, Y. Guillaneuf, C. Lefay, D. Bertin, D. Gigmes and B. Charleux, *Prog. Polym. Sci.*, 2013, **38**, 63–235.
17 R. Abbasi, A. Mitchell, P. G. Jessop and M. F. Cunningham, *RSC Appl. Polym.*, 2024, **2**, 214–223.
18 N. A. Rice, W. J. Bodnaryk, B. Mirka, O. A. Melville, A. Adronov and B. H. Lessard, *Adv. Electron. Mater.*, 2019, **5**, 1800539.
19 H. R. Lamontagne and B. H. Lessard, *ACS Appl. Polym. Mater.*, 2020, **2**, 5327–5344.
20 B. H. Lessard, X. Savelyeva and M. Marić, *Polymer*, 2012, **53**, 5649–5656.
21 M. Marić, *Can. J. Chem. Eng.*, 2021, **99**, 832–852.
22 B. Lessard and M. Marić, *Macromolecules*, 2010, **43**, 879–885.
23 G. Delaittre, J. Rieger and B. Charleux, *Macromolecules*, 2011, **44**, 462–470.
24 B. King and B. H. Lessard, *Macromol. React. Eng.*, 2017, **11**, 1600073.
25 B. Lessard and M. Marić, *Macromolecules*, 2008, **41**, 7870–7880.
26 A. Moayeri, B. Lessard and M. Maric, *Polym. Chem.*, 2011, **2**, 2084–2092.
27 B. Lessard, C. Tervo, S. De Wahl, F. J. Clerveaux, K. K. Tang, S. Yasmine, S. Andjelić, A. D'Alessandro and M. Marić, *Macromolecules*, 2010, **43**, 868–878.
28 C. Zhang, B. Lessard and M. Maric, *Macromol. React. Eng.*, 2010, **4**, 415–423.
29 N. B. Colthup, L. H. Daly and S. E. Wiberley, in *Introduction to Infrared and Raman Spectroscopy*, ed. N. B. Colthup, L. H. Daly and S. E. Wiberley, Academic Press, San Diego, 3rd edn, 1990, pp. 215–233.
30 D. A. Long, *J. Raman Spectrosc.*, 2005, **36**, 271.
31 J.-Y. Wang, F. Jin, X.-Z. Dong, J. Liu, M.-X. Zhou, T. Li and M.-L. Zheng, *Small*, 2023, **19**, 2303166.
32 Ch Hirschl, L. Neumaier, W. Mühleisen, M. Zauner, G. Oreski, G. C. Eder, S. Seufzer, Ch Berge, E. Rüland and M. Kraft, *Sol. Energy Mater. Sol. Cells*, 2016, **152**, 10–20.
33 O. Larsson, E. Said, M. Berggren and X. Crispin, *Adv. Funct. Mater.*, 2009, **19**, 3334–3341.
34 B. Ronnasi, B. King, S. Brixi, S. Swaraj, J. Niskanen and B. H. Lessard, *Adv. Electron. Mater.*, 2024, **10**, 2300810.
35 B. Mirka, N. A. Rice, P. Williams, M. N. Tousignant, N. T. Boileau, W. J. Bodnaryk, D. Fong, A. Adronov and B. H. Lessard, *ACS Nano*, 2021, **15**, 8252–8266.
36 B. Mirka, D. Fong, N. A. Rice, O. A. Melville, A. Adronov and B. H. Lessard, *Chem. Mater.*, 2019, **31**, 2863–2872.
37 M. N. Tousignant, N. A. Rice, J. Niskanen, C. M. Richard, D. Ritaine, A. Adronov and B. H. Lessard, *Adv. Electron. Mater.*, 2021, **7**, 2100700.
38 M. N. Tousignant, Z. S. Lin, J. Brusso and B. H. Lessard, *ACS Appl. Mater. Interfaces*, 2023, **15**, 3680–3688.
39 M. N. Tousignant, B. Ronnasi, V. Tischler and B. H. Lessard, *Adv. Mater. Interfaces*, 2023, **10**, 2300079.
40 B. Ronnasi, S. P. McKillop, M. Ourabi, M. Perry, H. A. Sharp and B. H. Lessard, *ACS Appl. Mater. Interfaces*, 2024, **16**, 65425–65435.
41 B. Ronnasi, M. N. Tousignant and B. H. Lessard, *J. Mater. Chem. C*, 2023, **11**, 3197–3205.
42 L. E. Dickson, S. Brixi, C. L. Radford, J. G. Manion, T. L. Kelly and B. H. Lessard, *J. Mater. Chem. C*, 2024, **12**, 17902–17912.
43 D. R. Nosov, B. Ronnasi, E. I. Lozinskaya, D. O. Ponkratov, L. Puchot, P. Grysan, D. F. Schmidt, B. H. Lessard and A. S. Shaplov, *ACS Appl. Polym. Mater.*, 2023, **5**, 2639–2653.
44 B. H. Lessard, E. J. Y. Ling and M. Marić, *Macromolecules*, 2012, **45**, 1879–1891.
45 A. J. Peltekoff, V. E. Hiller, G. P. Lopinski, O. A. Melville and B. H. Lessard, *ACS Appl. Polym. Mater.*, 2019, **1**, 3210–3221.